

# A high-dimensional orbital angular momentum entanglement measure

Isaac Nape,<sup>1</sup> Valeria Rodríguez-Fajardo,<sup>1</sup> Hsiao-Chih Huang,<sup>2</sup> and Andrew Forbes<sup>1</sup>

<sup>1</sup>*School of Physics, University of the Witwatersrand, Private Bag 3, Wits 2050, South Africa*

<sup>2</sup>*Department of Physics, National Taiwan University, Taipei 106, Taiwan*

Photons entangled in the orbital angular momentum (OAM) degree of freedom are promising candidates for accessing high-dimensional Hilbert spaces with the benefit of increasing the security and encoding capacity of quantum systems. While it is possible to witness high-dimensional entanglement and obtain bounds on the dimensions, quantifying the dimensionality of OAM entanglement remains an open challenge. Here we report a measurement scheme that returns the dimensionality of OAM entangled photons by simple projective measurements. We achieve this by engineering superpositions of fractional OAM modes such that the resulting azimuthal phase has  $n$  identical discontinuities. We show that a simple conditional measurement, akin to a Bell measurement, returns a visibility that scales monotonically with entanglement dimensionality, allowing for a quantitative measurement of the quantum state's dimension. Our approach overcomes the present hurdles of arduous quantum state tomographies as well as fair sampling violations in Bell measurements, providing a simple and direct dimensionality measure of entangled OAM states.

The transverse spatial modes of photons carrying orbital angular momentum (OAM) have provided a means to realising quantum entanglement beyond qubits [1–7]. They have emerged as an ideal resource in quantum information processing and communication, including superdense coding [8, 9], multi-photon entanglement [10], quantum teleportation [11] and entanglement swapping [12, 13], ghost imaging [14–16] and secure communication in free-space [17, 18] and optical fibre [19–22], fuelled by their inherent advantages such as robustness against noise [23] and higher information capacity per photon [24]. Further, the toolkit to engineer high-dimensional states is readily available, e.g., by linear [25] and non-linear processes [26–30], with up to  $100 \times 100$  dimensions already demonstrated [31].

Despite these advances, certifying and quantifying the dimensionality of such systems still remains challenging. The intuitive approach of simply measuring the width of the OAM spiral spectrum (OAM bandwidth) is a necessary but not sufficient condition to determine dimensionality as it fails to account for non-local correlations. Consequently, many techniques have been developed to witness, bound and attempt to quantify high-dimensional OAM quantum states. These include single shot measurements of the OAM spectrum [32, 33], approximating the density matrix via quantum state tomography (QST) with multiple qubit state projections [34], using mutually unbiased bases [35, 36] to probe the states, and testing non-local bi-photon correlations by generalised Bell tests in higher dimensions [37–44]. However, the spectrum measurements do not confirm entanglement, the QST approach scales unfavourably with dimension, only bounds or witnesses are possible with the probes and the dimension must be known *a priori* (e.g., valid for prime or prime power dimensions), while the high-dimensional Bell tests often fail the fair sampling condition [45, 46], invalidating the technique for general states.

Here we present a robust scheme that exploits the multi-modal nature of fractional OAM modes to quantify the dimensionality of an entangled OAM state. In

our approach, we engineer high dimensional OAM analysers from  $n$  odd superpositions of fractional OAM modes with a half integer charge. This allows us to measure coincidence fringes from relative rotations of the analysers acting on the entangled photons, akin to a Bell measurement. From the visibility of the curves, only reproducible by entangled photons, we can infer the dimensionality of our entangled state quantitatively. We outline the concept theoretically and demonstrate it experimentally.

## I. METHOD DESCRIPTION

The task here is to measure the dimensions of an entanglement system defined in the OAM basis where each photon's transverse mode, denoted by the state  $|\ell\rangle$ , is associated with an azimuthal phase profile  $\exp(i\ell\phi)$ , with  $\ell \in \mathbb{Z}$  the topological charge and  $\ell\hbar$  OAM per photon. In a typical experiment, illustrated in Fig. 1 (a), a Gaussian pump photon initiates a spontaneous parametric downconversion (SPDC) process to produce the bi-photon state

$$|\Psi\rangle = \sum_{\ell=-L}^L \lambda_{\ell} |\ell\rangle_A |-\ell\rangle_B, \quad (1)$$

where  $L$  is a positive integer, and  $|\lambda_{\ell}|^2$  is the probability of generating photons in the states  $|\pm\ell\rangle$  for photon A and B, respectively. The distribution of  $|\lambda_{\ell}|^2$ , with examples shown in Fig. 1 (b), relates directly to the width of the OAM entangled spectrum,  $\Delta\ell$ , (two times the standard deviation of the distribution) and the Schmidt number,  $K$ , which in turn is associated with the dimensionality of  $|\Psi\rangle$ . For example, a  $d$ -dimensional maximally entangled state has an OAM spectrum that is uniformly distributed,  $|\lambda_{\ell}|^2 = d^{-1} = (2L+1)^{-1}$ , resulting in  $\Delta\ell = L+1$  and  $K = 2d+1$  (see Supplementary Information for further examples and details). We wish to infer  $K$  and  $\Delta\ell$ , and therefore  $d$ , for some bi-photon state, making use of fractional OAM mode projectors. We outline

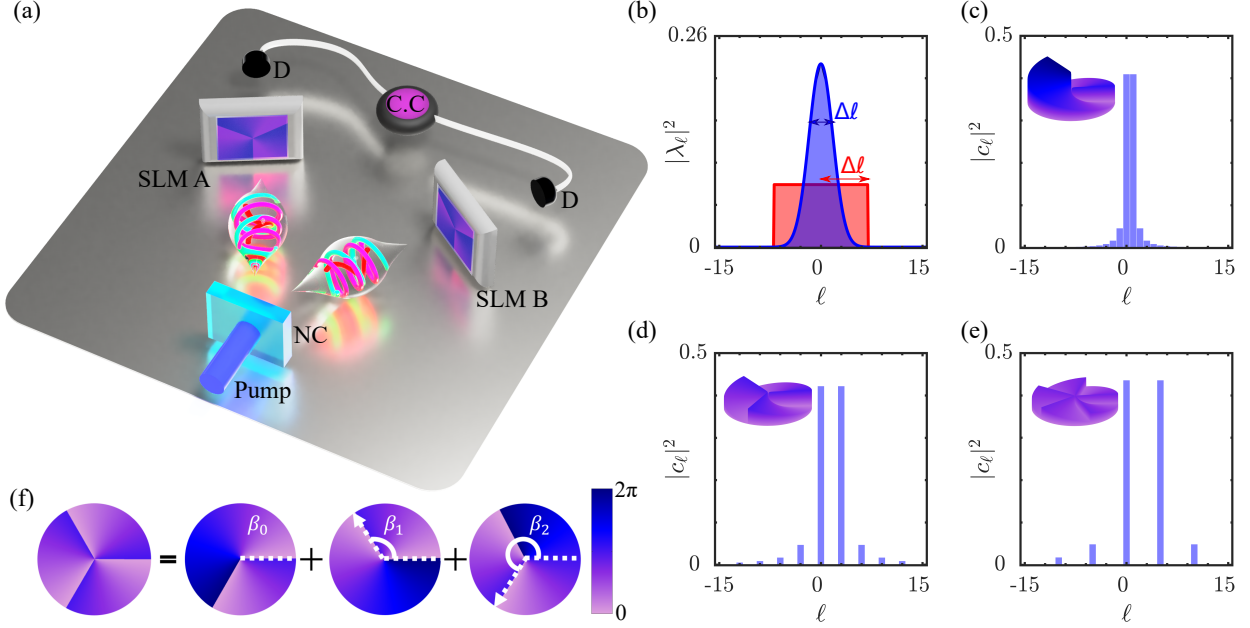


FIG. 1. **Conceptual sketch of the optical setup and mode spectrum of tailored analysers.** (a) Conceptual two photon entanglement experiment where a high energy photon (Pump) is converted into two spatially entangled photons in a non-linear crystal (NC). The photons are then measured separately in two arms, A and B, using spatial light modulators (SLMs) before finally collected by single mode fibers coupled to single photon detectors (D) and time correlated using a coincidence counter (C.C). (b) Examples of spiral spectra for a maximally entangled state and non uniform spectrum. (c) The OAM spectrum of a single fractional ( $|M, \alpha\rangle_n = |0.5, 0\rangle$ ), with superposition states (d)  $|M, \alpha\rangle_n = |1.5, 0\rangle_3$  and (e)  $|M, \alpha\rangle_n = |2.5, 0\rangle_5$  of our tailored analysers. (f) Example superposition to generate the fractional spiral phase profile projecting onto the state  $|M, \alpha\rangle_n = |1.5, 0\rangle_3$ . Here  $\beta_k = \frac{2\pi}{n}k$ , with  $k = 0, \dots, n-1$ , is the position corresponding to the edge dislocation of the  $k$ th analyser relative to its initial position  $\alpha = 0$ .

the concept here, with full details in the Supplementary Information. Fractional OAM modes are spatial modes with a non-integer average OAM [43]. Initially, these modes were discovered through the use of single spiral phase plates (SPPs) with a non-integer phase step and later generalized to multiple plates [47]. Their phase profile is characterised by a phase discontinuity situated at an orientation angle,  $\alpha$ . A single fractional mode projector has a transmission function

$$\exp(i\Phi) = e^{iM\phi} \begin{cases} e^{iM(2\pi-\alpha)} & 0 \leq \phi < \alpha \\ e^{iM(-\alpha)} & \alpha \leq \phi < 2\pi \end{cases}, \quad (2)$$

where  $\phi$  is the azimuth coordinate and  $M = m + \mu$  is the fractional OAM made up of an integer,  $m \in \mathbb{Z}$ , and non-integer part,  $\mu \in (0, 1)$ . In the OAM basis we can write this as  $|M, \alpha\rangle = \sum_{\ell} c_{\ell, M}(\alpha) |\ell\rangle$  with a spectrum given by  $c_{\ell, M}$ .

For our approach to work effectively, we need to have control over the OAM mode spectrum (amplitudes and phases) that we test for, and so we use a superposition of  $n$  such projectors given by

$$|M, \alpha\rangle_n = \mathcal{N} \sum_{k=0}^{n-1} |M, \beta_k \oplus \alpha\rangle, \quad (3)$$

where  $\mathcal{N}$  is a normalization constant. Each fractional mode in this superposition has the same charge,  $M$ , but is rotated by an angle  $\beta_k \oplus \alpha = \text{mod}\{\beta_k + \alpha, 2\pi\}$  for  $\beta_k = \frac{2\pi}{n}k$ , as illustrated in Fig. 1 (f). This means that the average OAM of each contributing fractional mode is kept constant and only the angular position of the edge dislocation rotates by an angle of  $\beta_k$  with respect to the initial position,  $\alpha$ . Although the average OAM is invariant with respect to the phase gradient  $M$ , the spectrum is not: it has been tailored in amplitude and phase to

$$c_{\ell, M}^n(\alpha) = \mathcal{N} \exp(-i\pi\ell(n-1)/n) A_{\ell}^n c_{\ell, M}(\alpha), \quad (4)$$

with

$$A_{\ell}^n = \begin{cases} 1, & \text{mod}\left\{\frac{1}{2}\ell\beta_{n-1}, 2\pi\right\} = 0 \\ 0, & \text{otherwise} \end{cases}. \quad (5)$$

The overlap probabilities are then  $P_{\ell}^n = |\mathcal{N} A_{\ell}^n c_{\ell}|^2$ , so that the new spectrum has the same amplitude as before,  $|c_{\ell, M}|^2$ , but modulated by the selection rule  $A_{\ell}^n$ . This new spectrum can be tuned by carefully selecting  $n$ , therefore enabling precise control of the OAM subspaces. The theoretical spectra of the analysers  $|M, \alpha\rangle_n = |1.5, 0\rangle_{1,3,5}$  are presented in Fig. 1 (c), (d) and (e), respectively. Interestingly, the superpositions with  $n > 1$  have a sparse distribution in  $\ell$ , with the spacing

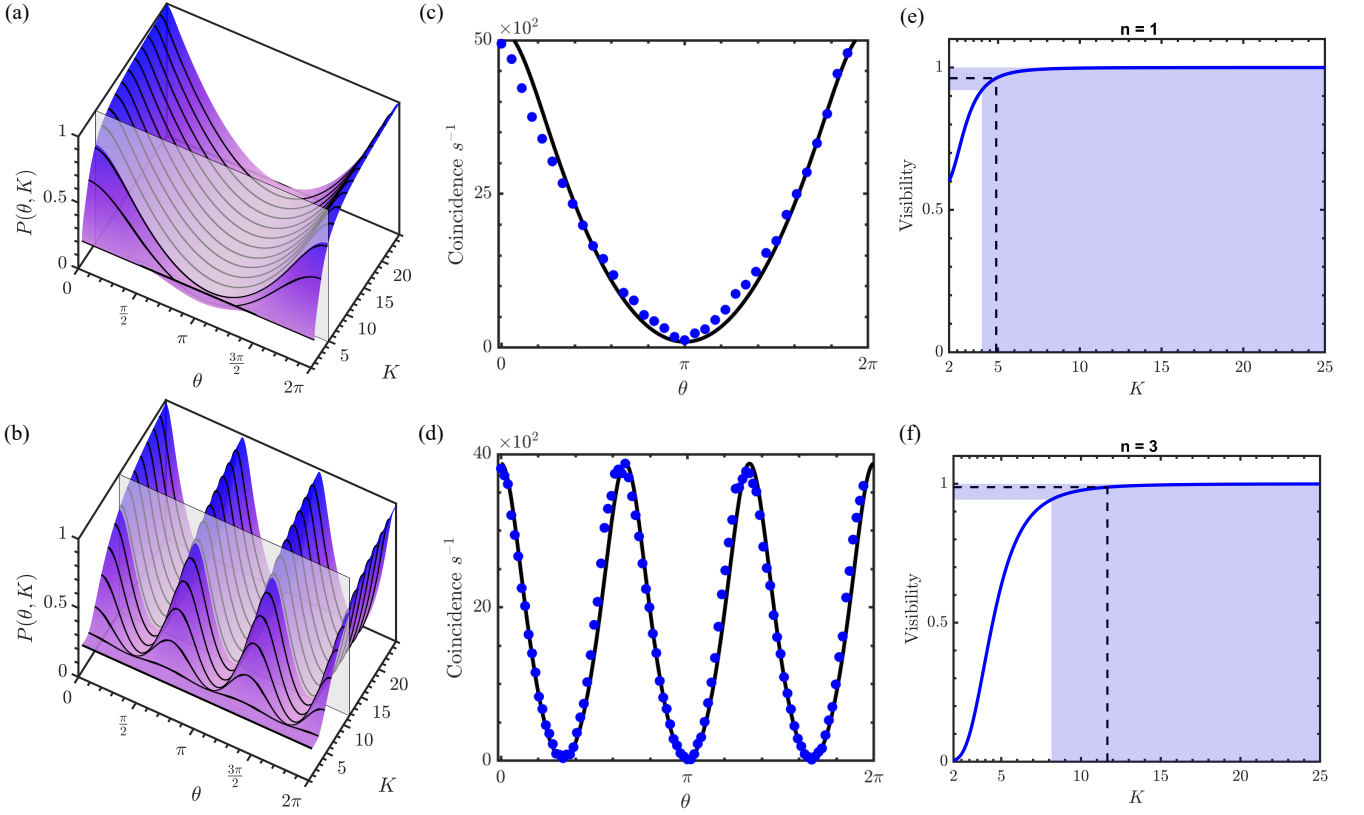


FIG. 2. **Theoretical and experimental detection probabilities using superpositions of fractional OAM modes.** Simulated probability curves determined from the overlap  $\langle 0, M|_n \langle \theta, -M|_n |\Psi \rangle$  for (a)  $n = 1$ , (b)  $n = 3$  with fractional OAM of  $M=1.5$  in both cases. Here  $\theta$  is the relative orientation of the analysers while  $K$  is the OAM dimensionality of the entangled photons. Experimental (points) and theoretical (solid lines) coincidence counts rates between fractional OAM mode analysers when (c)  $n = 1$  and (d)  $n = 3$  with fractional OAM of  $M = 1, 5$  for both cases, respectively. These correspond to inferred dimensions of  $K = 4.89 \pm 13.28$  and  $K = 11.68 \pm 2.42$ , respectively. The visibility vs Schmidt number ( $K$ ) determined from the probabilities ( (a) and (b) ) curves for (e)  $n = 1$  and (f)  $n = 3$ . The dotted lines correspond to the measured visibility (horizontal) and inferred dimensions (vertical) while the shaded area is corresponds to the range (between the upper and lower limit) of  $K$  values found within an absolute error tolerance of 0.05 between the experiment and theory.

between two consecutive  $\ell$ s with non-zero probability  $P_\ell^n$  given by  $n$ .

Next, we wish to project each photon in the SPDC state of Eq. (1) onto identical but conjugated fractional OAM states orientated by an angle  $\theta$  relative to one another. The outcome probability of such a measurement, i.e.,  $|\langle 0, M|_n \langle \theta, -M|_n |\Psi \rangle|^2$ , is

$$P_n(\theta) = \left| \sum_{\ell=-\infty}^{\infty} \lambda_\ell (c_{\ell, M}^n(0) c_{-\ell, -M}^n(\theta))^* \right|^2, \quad (6)$$

where  $\lambda_\ell$  is the initial bi-photon OAM spectrum and  $\theta$  the relative rotation angle of the two analysers. Although not immediately obvious,  $\Delta\ell$  and  $K$  can be inferred from this probability distribution owing to their dependence on  $\lambda_\ell$ . Specifically, the measurement of  $P_n(\theta)$  depending on the relative orientation  $\theta$  of two conjugate analysers results in coincidence fringes, whose visibility  $V_n(M)$  can be used to determine the system degree of entanglement. We chose odd values of  $n$  with  $M = n/2$  since this pro-

duces a high visibility  $V = 1$  for a maximally entangled state (see details in the Supplementary Information). In general, both the shape and visibility of the fringes yield information about the state. In Fig. 2 (a) and (b), we show the calculated detection probabilities of such a measurement using Eq. (6), as function of  $\theta$  and dimensions  $K$  for  $M = 1.5$  and  $n = 1$  and 3, respectively. We assumed the spectrum of the modes to be symmetric and found convenient to model it as a normal distribution. Examples of the probabilities for a fixed  $K$  taken for each  $n = 1$  and 3 superposition are shown Fig. 2 (c) and (d), illustrating the periodic nature of the probabilities with  $\theta$ . We demonstrate the impact of dimensions on the expected visibilities (continuous lines) in Fig. 2 (e) and Fig. 2 (f) for the  $n = 1, 3$ . The visibilities increases monotonically with  $K$  for each analyser.

Since the visibilities reveal information about the same quantum systems but in differing subspaces, we introduce

the parameter

$$W_N = \sum_{k=1}^N V_{2k-1}(M), \quad (7)$$

summed over all  $n = 2k - 1$  superposition states up to some maximum number of modes  $n = 2N - 1$  in the superposition projection, i.e., the last analyser used would be  $|M, \alpha\rangle_{2N-1}$ . It provides a compact way of quantifying the degree of entanglement in the system. For each analyser, the visibility increases monotonically with  $K$ , therefore  $W_N$  produces a monotonically increasing function, from which the dimensionality of the entangled state can be read off (see Supplementary Information for the detailed procedure). The scheme can be summarised as follows: First, measure coincidence fringes  $P_n(\theta)$  for various fractional superpositions  $n$  up to some desired number  $N$ . Second, compute the parameter  $W_N$  and, third, from this calculate the dimensionality by numerical inversion of  $W_N$  with respect to the entanglement dimensions  $K$ . Note that  $K$  is calculated from the weightings of the model distribution (see Supplementary Information).

## II. RESULTS

The set-up used to demonstrate our scheme is shown conceptually in Fig. 1 (a) with the corresponding detailed schematic in the Methods section. To test that our analysers tailor the spiral spectrum as predicted in Eq. (4), we projected one photon onto a fractional OAM (superposition) state and the other onto an OAM state; the results are given in the Supplementary Information, and confirm the validity of the holograms. Next, we perform the key measurement: coincidences between the signal and idler photons for fractional projections on both arms as a function of the relative rotation angle of the holograms. To achieve this, we encoded the fractional OAM mode analyser on the SLM in signal arm fixed at an angle of 0 while the conjugate mode was rotated at angles  $\theta \in [0, 2\pi]$ . Examples of the detection probabilities for a fixed  $K$  taken for superpositions  $n = 1$  and 3, and charges  $M = 1.5$  (in both cases) are shown in Fig. 2 (b) and (c), illustrating the periodic nature of the probabilities with  $\theta$ . We measured high visibilities of  $V = 0.96 \pm 0.04$  and  $V = 0.98 \pm 0.01$ . The multiple peaks in Fig. 2 (b) confirm the azimuthal  $n$ -fold symmetry of the analysers imprinted in the frequency of the detected probability fringes as predicted by the theory.

In order to demonstrate the impact of the dimensionality on the measured visibilities we use four projectors of  $n = 1, 3, 5$  and 7, with  $M = n/2$  for each case. Firstly, we show that the upper and lower bounds of the dimensionality,  $K$ , in combination with the uncertainty,  $\Delta K$ , can be minimised by iterating through the  $n$  the superposition measurements. In Fig. 2 (e) and (f) we show the theoretical visibilities for analysers  $n = 1$  and 3 as a function of the Schmidt number  $K$  (continuous

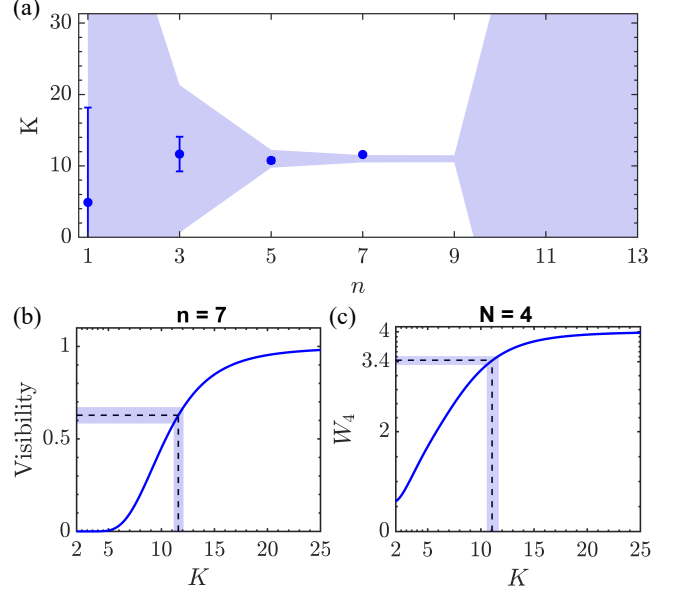


**FIG. 3. Quantifying the entanglement dimensionality from the measured visibilities.** (a) Dimensionality ( $K$ ) versus the number of superpositions ( $n$ ). The shaded area corresponds to the calculated theoretically uncertainty  $\Delta K$  for  $\Delta V = 0.05$  centred around  $K = 11.5$ , and the points to the experimental values. (b) Measured (dashed line) and simulated (continuous line) visibility as a function of  $K$  for projections with  $n = 7$  superpositions with a measured visibility of  $V = 0.63 \pm 0.02$ , we infer  $K = 11.59 \pm 0.23$ . The shaded area corresponds to  $K$  values within the upper and lower bounds of  $K$ . (c) Measurement of the entanglement dimensions from the  $W_N$  parameter: a measured  $W_4 = 3.42 \pm 0.09$  corresponds to a dimensionality of  $K = 11.05 \pm 0.30$ . All uncertainties are quoted as standard deviations.

lines), and marked as horizontal dashed lines the experimentally measured values from Fig. 2 (c) and (d). The shaded region corresponds to the area bounded by the upper and lower limits of  $K$ ,  $K_{\text{upper}} = K_n(V + \Delta V)$  and  $K_{\text{lower}} = K_n(V - \Delta V)$ , for the inferred dimensionality,  $K_n$ , with an error tolerance  $\Delta V = 0.05$ . The bounds yield finite values when  $|1 - V_{\text{measured}, n}| > \Delta V$ , so that the width,  $|K_{\text{upper}} - K_{\text{lower}}|$ , decreases with iterations of the  $n$  superpositions. Conversely, the upper limit of  $K_n$  is much larger and as a consequence the width,  $|K_{\text{upper}} - K_{\text{lower}}|$ , is also large. This is primarily due to the fact that  $\frac{d}{dK}V(K) \approx 0$  as  $K$  increases. We associate the uncertainty of the measured  $K$  with the standard deviation  $\Delta K = (\frac{dV}{dK})^{-1}\Delta V$ , which we find also decreases with increasing  $n$ . Since both the width,  $|K_{\text{upper}} - K_{\text{lower}}|$ , of  $K$  as well as the uncertainty,  $\Delta K$  (standard deviation), decrease with  $n$ , we can confidently confirm entanglement dimensions of our system. We illustrate these two key findings graphically in Fig. 3 (a) for simulated (shaded) and experimental (points) results in terms of the uncertainty, and confirmed the reduction in the difference between the upper and lower bounds of



$K$  in Fig. 3 (b) for  $n = 7$ .

Although increasing  $n$  yields the desired result, it decreases the coincidences in the experiment. We therefore use  $W_4$  (for the four analysers used) which is a sum over the measured visibilities and increases monotonically with  $K$ . This is illustrated in Fig. 3 (c) for both experiment (horizontal line) and theory (continuous line). We infer from our measurements  $W_4 = 3.42 \pm 0.09$ , yielding  $K = 11.05 \pm 0.30$  (see Supplementary Information) consistent with the result directly from the visibility of  $K = 11.59 \pm 0.23$  for  $n = 7$ . Since in our controlled experiment we do in fact have prior knowledge of our SPDC state, we can perform a sanity check by comparing our results to that directly inferred from the spiral spectrum, namely,  $K = 15$  and corresponding  $\Delta\ell = 9.42$ . We see that the spiral spectrum over-estimates the dimensionality.

### III. DISCUSSION AND CONCLUSION

High dimensional spatial mode entanglement, particularly in the OAM degree of freedom, has many potential benefits that can be used to boost the information capacity of various quantum protocols. In most lab environments, measuring the bandwidth, or equivalently dimensionality, of an entanglement system in a controllable way is an essential step. However, this is not an easy task since the OAM state space is unbounded. The best approaches to date rely on Bell violations [39] or projections with multiple mutual unbiased bases [35, 36], imposing conditions on the dimensions to be tested for and do not provide a direct measure for dimensionality. In this paper, we presented a solution to this problem.

We demonstrated a technique to directly measure the dimensionality of an entanglement system. We achieved this by engineering superpositions of fractional OAM modes resulting in OAM superposition states with controllable phases and amplitudes. By encoding two of these analysers as holograms on SLMs inserted on separate paths of entangled photons, periodic probability fringes were observed as a function of their relative rotation. Our theoretical model reveals that the visibility of the coincidences fringes is monotonically increasing with the dimensionality of the system, therefore we exploit this property to measure the dimensionality in a fast and simple manner.

Unlike a conventional Schmidt decomposition in the OAM basis, the bandwidth extracted from our technique requires coherence over many modes. Therefore, a maximally mixed entangled system cannot yield the same result. Moreover, since each analyser projects onto  $d > 2$  dimensions, few measurements are required as compared to methods that project onto multiple qubit superpositions [31]. Furthermore, while our technique is similar to the one used for Shannon dimensionality [40], i.e., by using coincidence fringes obtained from measurements with angular phase masks, our method is not limited by the

modal spectrum of the analysers because we have better control of the mode selection for each analyser.

In summary, we have presented a simple yet powerful technique to quantitatively measure the dimensionality of OAM entangled photons. Our approach requires no *a priori* knowledge of the state, is robust, fast, and provides a measure on dimensionality rather than a bound or a witness. While our scheme exploits visibility in fringes after joint fractional projections, it is not based on a Bell inequality violation and thus overcomes the fair sampling issue inherent in related approaches. We believe that this tool will be useful to the active research in high-dimensional spatial mode entanglement using the OAM as a basis.

### ACKNOWLEDGEMENTS

The authors express their gratitude to Bienvenue Ndagano and Feng Zhu for their useful advice and insight. I.N. acknowledges financial support from the Department of Science and Technology (South Africa).

### AUTHOR CONTRIBUTIONS

The experiment was performed by I.N. and V.F., the theory was developed by I.N. and H.H., the data analysis was performed by I.N., V.F. and A.F. and the experiment was conceived by A.F. All authors contributed to the writing of the manuscript.

### METHODS

#### Holographic fractional OAM mode projections.

The conventional method for generating fractional OAM modes involves imprinting an azimuthally dependent phase retardation onto an incoming field with spiral phase plates [48] or digital holograms [49]. Here, we employed dynamic phase control with liquid crystal spatial light modulators (SLMs) [50] to generate rotated fractional OAM phase masks to modulate the transverse plane of photons. We achieved this by preparing grey-scale holograms encoded with the phase profile (see Fig. 4 (a)-(d)) of a transmission function corresponding to the desired projection mode. Accordingly, we prepared holograms with superpositions of multiple rotated fractional spiral phases having a transmission function,  $T_n(\alpha, \phi) = \langle \phi | M_n(\alpha, \phi) \rangle$ , where  $\phi$  is the azimuthal coordinate given by  $\phi = \tan^{-1}(\frac{y}{x})$ , where  $(x, y)$  are the coordinates of each pixel. We generated holograms with the desired phase and subsequently added them to a blazed grating for a final hologram mapped as

$$\Phi_{\text{SLM}}(x, y) = \text{mod} \{ \arg(T_n(\alpha, \phi)) + G_x x + G_y y, 2\pi \}, \quad (8)$$

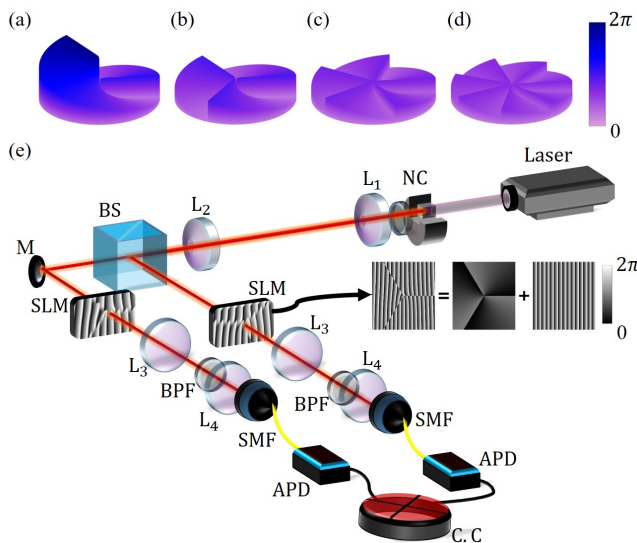


FIG. 4. **Experimental setup.** (a)-(d) Phase profiles of fractional OAM analysers for  $n = 1, 2, 3$ , and  $4$ , all with charges  $M = n/2$ , respectively. (e) Experimental setup. SLM: spatial light modulator; L: lens; NC: nonlinear crystal; BS: beam splitter; M: mirror; SMF: single mode fibre; APD: avalanche photodiode; BPF: bandpass filter; s: signal; i: idler; C.C: coincidence counter. Inset: illustration of the hologram generation.

where  $G_{x,y}$  are the grating wavenumbers in the  $x$  and  $y$  directions, respectively. An example of the phase hologram generated of a superposition of three fractional OAM spiral phases ( $n = 3$  with  $M = 1.5$ ) is shown in the insert of Fig. 4 (e).

**Experimental setup for measurements on down-conversion photons.** The experimental setup for the generation and measurement of entangled photons is illustrated in Fig. 4 (e). A potassium-titanium-phosphate (PPKTP) type I nonlinear crystal was pumped with a 405 nm wavelength diode laser. The crystal temperature was set to obtain co-linear signal and idler entangled SPDC photons centred at a wavelength 810 nm. The photon pairs were then separated in path using a 50:50 beam splitter (BS). Each entangled photon was imaged onto a spatial light modulator (SLM) using a  $4f$  telescope ( $f_1$  and  $f_2$  having focal lengths of 100 mm and 500 mm, respectively), then subsequently coupled into single mode fibers with a second  $4f$  telescope (lenses  $f_3$  and  $f_4$  having focal lengths of 750 mm and 2 mm, respectively) and finally detected with avalanche photo-detectors (APDs). Signals from each arm were measured in coincidences within a 25 ns coincidence window. The entangled photons were filtered with 10 nm bandpass filters (BPFs) centered at a wavelength of 810 nm. For our experimental demonstration, we restrict our measurements to a fixed  $\Delta\ell = 9.42$  and corresponding FWHM of 11.09. That is, the dimensionality of the source are kept constant. Moreover we measure visibility against  $n$  to show the impact of using our analysers for measuring high dimensional correlations and confirmed our measurements with the theoretical predictions.

- 
- [1] R. Fickler, R. Lapkiewicz, W. N. Plick, M. Krenn, C. Schaeff, S. Ramelow, and A. Zeilinger, “Quantum entanglement of high angular momenta,” *Science*, vol. 338, no. 6107, pp. 640–643, 2012.
  - [2] M. Krenn, J. Handsteiner, M. Fink, R. Fickler, and A. Zeilinger, “Twisted photon entanglement through turbulent air across vienna,” *Proceedings of the National Academy of Sciences*, vol. 112, no. 46, pp. 14197–14201, 2015.
  - [3] M. Erhard, M. Malik, and A. Zeilinger, “A quantum router for high-dimensional entanglement,” *Quantum Science and Technology*, vol. 2, no. 1, p. 014001, 2017.
  - [4] M. Erhard, R. Fickler, M. Krenn, and A. Zeilinger, “Twisted photons: new quantum perspectives in high dimensions,” *Light: Science & Applications*, vol. 7, no. 3, pp. 17146–17146, 2018.
  - [5] R. Fickler, R. Lapkiewicz, M. Huber, M. P. Lavery, M. J. Padgett, and A. Zeilinger, “Interface between path and orbital angular momentum entanglement for high-dimensional photonic quantum information,” *Nature communications*, vol. 5, no. 1, pp. 1–6, 2014.
  - [6] A. Forbes and I. Nape, “Quantum mechanics with patterns of light: Progress in high dimensional and multi-dimensional entanglement with structured light,” *AVS Quantum Science*, vol. 1, no. 1, p. 011701, 2019.
  - [7] G. Molina-Terriza, J. P. Torres, and L. Torner, “Twisted photons,” *Nature Physics*, vol. 3, no. 5, pp. 305–310, 2007.
  - [8] C. Wang, F.-G. Deng, Y.-S. Li, X.-S. Liu, and G. L. Long, “Quantum secure direct communication with high-dimension quantum superdense coding,” *Physical Review A*, vol. 71, no. 4, p. 044305, 2005.
  - [9] J. T. Barreiro, T.-C. Wei, and P. G. Kwiat, “Beating the channel capacity limit for linear photonic superdense coding,” *Nature physics*, vol. 4, no. 4, p. 282, 2008.
  - [10] M. Malik, M. Erhard, M. Huber, M. Krenn, R. Fickler, and A. Zeilinger, “Multi-photon entanglement in high dimensions,” *Nature Photonics*, vol. 10, pp. 248–252, 2016.
  - [11] S. K. Goyal, P. E. Boukama-Dzoussi, S. Ghosh, F. S. Roux, and T. Konrad, “Qudit-teleportation for photons with linear optics,” *Scientific reports*, vol. 4, p. 4543, 2014.
  - [12] Y. Zhang, M. Agnew, T. Roger, F. S. Roux, T. Konrad, D. Faccio, J. Leach, and A. Forbes, “Simultaneous entanglement swapping of multiple orbital angular momentum states of light,” *Nature Communications*, vol. 8, no. 1, p. 632, 2017.
  - [13] N. Bornman, M. Agnew, F. Zhu, A. Vallés, A. Forbes,

- and J. Leach, “Ghost imaging using entanglement-swapped photons,” *npj Quantum Information*, vol. 5, no. 1, pp. 1–6, 2019.
- [14] B. Jack, J. Leach, J. Romero, S. Franke-Arnold, M. Ritsch-Marte, S. M. Barnett, and M. J. Padgett, “Holographic ghost imaging and the violation of a bell inequality,” *Phys. Rev. Lett.*, vol. 103, p. 083602, 2009.
- [15] L. Chen, J. Lei, and J. Romero, “Quantum digital spiral imaging,” *Light: Science & Applications*, vol. 3, no. 3, pp. e153–e153, 2014.
- [16] N. Bornman, S. Prabhakar, A. Vallés, J. Leach, and A. Forbes, “Ghost imaging with engineered quantum states by hong-ou-mandel interference,” *New Journal of Physics*, vol. 21, no. 7, p. 073044, 2019.
- [17] M. Mafu, A. Dudley, S. Goyal, D. Giovannini, M. McLaren, M. J. Padgett, T. Konrad, F. Petruccione, N. Lütkenhaus, and A. Forbes, “Higher-dimensional orbital-angular-momentum-based quantum key distribution with mutually unbiased bases,” *Physical Review A*, vol. 88, no. 3, p. 032305, 2013.
- [18] F. Steinlechner, S. Ecker, M. Fink, B. Liu, J. Bavaresco, M. Huber, T. Scheidl, and R. Ursin, “Distribution of high-dimensional entanglement via an intra-city free-space link,” *Nature communications*, vol. 8, p. 15971, 2017.
- [19] J. Liu, I. Nape, Q. Wang, A. Vallés, J. Wang, and A. Forbes, “Multidimensional entanglement transport through single-mode fiber,” *Science advances*, vol. 6, no. 4, p. eaay0837, 2020.
- [20] H. Cao, S.-C. Gao, C. Zhang, J. Wang, D.-Y. He, B.-H. Liu, Z.-W. Zhou, Y.-J. Chen, Z.-H. Li, S.-Y. Yu, *et al.*, “Distribution of high-dimensional orbital angular momentum entanglement over a 1 km few-mode fiber,” *Optica*, vol. 7, no. 3, pp. 232–237, 2020.
- [21] D. Cozzolino, E. Polino, M. Valeri, G. Carvacho, D. Bacco, N. Spagnolo, L. K. Oxenløwe, and F. Sciarrino, “Air-core fiber distribution of hybrid vector vortex-polarization entangled states,” *Advanced Photonics*, vol. 1, no. 4, p. 046005, 2019.
- [22] D. Cozzolino, D. Bacco, B. Da Lio, K. Ingerslev, Y. Ding, K. Dalgaard, P. Kristensen, M. Galili, K. Rottwitt, S. Ramachandran, *et al.*, “Orbital angular momentum states enabling fiber-based high-dimensional quantum communication,” *Physical Review Applied*, vol. 11, no. 6, p. 064058, 2019.
- [23] S. Ecker, F. Bouchard, L. Bulla, F. Brandt, O. Kohout, F. Steinlechner, R. Fickler, M. Malik, Y. Guryanova, R. Ursin, *et al.*, “Overcoming noise in entanglement distribution,” *Physical Review X*, vol. 9, no. 4, p. 041042, 2019.
- [24] J. Leach, E. Bolduc, D. J. Gauthier, and R. W. Boyd, “Secure information capacity of photons entangled in many dimensions,” *Physical Review A*, vol. 85, no. 6, p. 060304, 2012.
- [25] Y. Zhang, F. S. Roux, T. Konrad, M. Agnew, J. Leach, and A. Forbes, “Engineering two-photon high-dimensional states through quantum interference,” *Science Advances*, vol. 2, no. 2, p. e1501165, 2016.
- [26] J. Torres, A. Alexandrescu, and L. Torner, “Quantum spiral bandwidth of entangled two-photon states,” *Physical Review A*, vol. 68, no. 5, p. 050301, 2003.
- [27] F. M. Miatto, A. M. Yao, and S. M. Barnett, “Full characterization of the quantum spiral bandwidth of entangled biphotons,” *Physical Review A*, vol. 83, no. 3, p. 033816, 2011.
- [28] J. Romero, D. Giovannini, S. Franke-Arnold, S. M. Barnett, and M. J. Padgett, “Increasing the dimension in high-dimensional two-photon orbital angular momentum entanglement,” *Phys. Rev. A*, vol. 86, p. 012334, Jul 2012.
- [29] G. Molina-Terriza, J. P. Torres, and L. Torner, “Management of the angular momentum of light: Preparation of photons in multidimensional vector states of angular momentum,” *Phys. Rev. Lett.*, vol. 88, p. 013601, Dec 2001.
- [30] Y. Zhang, M. McLaren, F. S. Roux, and A. Forbes, “Simulating quantum state engineering in spontaneous parametric down-conversion using classical light,” *Optics Express*, vol. 22, no. 14, pp. 17039–17049, 2014.
- [31] M. Krenn, M. Huber, R. Fickler, R. Lapkiewicz, S. Ramelow, and A. Zeilinger, “Generation and confirmation of a  $(100 \times 100)$ -dimensional entangled quantum system,” *Proceedings of the National Academy of Sciences*, vol. 111, no. 17, pp. 6243–6247, 2014.
- [32] H. D. L. Pires, H. C. B. Florijn, and M. P. van Exter, “Measurement of the spiral spectrum of entangled two-photon states,” *Phys. Rev. Lett.*, vol. 104, p. 020505, 2010.
- [33] G. Kulkarni, R. Sahu, O. S. Magaña-Loaiza, R. W. Boyd, and A. K. Jha, “Single-shot measurement of the orbital-angular-momentum spectrum of light,” *Nature communications*, vol. 8, no. 1, pp. 1–8, 2017.
- [34] M. Agnew, J. Leach, M. McLaren, F. S. Roux, and R. W. Boyd, “Tomography of the quantum state of photons entangled in high dimensions,” *Physical Review A*, vol. 84, p. 062101, 2011.
- [35] D. Giovannini, J. Romero, J. Leach, A. Dudley, A. Forbes, and M. J. Padgett, “Characterization of high-dimensional entangled systems via mutually unbiased measurements,” *Physical Review Letters*, vol. 110, no. 14, p. 143601, 2013.
- [36] J. Bavaresco, N. H. Valencia, C. Klöckl, M. Pivoluska, P. Erker, N. Friis, M. Malik, and M. Huber, “Measurements in two bases are sufficient for certifying high-dimensional entanglement,” *Nature Physics*, pp. 1745–2481, 2018.
- [37] A. Vaziri, G. Weihs, and A. Zeilinger, “Experimental two-photon, three-dimensional entanglement for quantum communication,” *Physical Review Letters*, vol. 89, no. 24, p. 240401, 2002.
- [38] S. Gröblacher, T. Jennewein, A. Vaziri, G. Weihs, and A. Zeilinger, “Experimental quantum cryptography with qutrits,” *New Journal of Physics*, vol. 8, no. 5, p. 75, 2006.
- [39] A. C. Dada, J. Leach, G. S. Buller, M. J. Padgett, and E. Andersson, “Experimental high-dimensional two-photon entanglement and violations of generalized bell inequalities,” *Nature Physics*, vol. 7, no. 9, p. 677, 2011.
- [40] J. Pors, S. Oemrawsingh, A. Aiello, M. Van Exter, E. Eliel, J. Woerdman, *et al.*, “Shannon dimensionality of quantum channels and its application to photon entanglement,” *Physical review letters*, vol. 101, no. 12, p. 120502, 2008.
- [41] S. Oemrawsingh, X. Ma, D. Voigt, A. Aiello, E. t. Eliel, J. Woerdman, *et al.*, “Experimental demonstration of fractional orbital angular momentum entanglement of two photons,” *Physical review letters*, vol. 95, no. 24, p. 240501, 2005.

- [42] S. Oemrawsingh, J. de Jong, X. Ma, A. Aiello, E. Eliel, J. Woerdman, *et al.*, “High-dimensional mode analyzers for spatial quantum entanglement,” *Physical Review A*, vol. 73, no. 3, p. 032339, 2006.
- [43] J. B. Götte, S. Franke-Arnold, R. Zambrini, and S. M. Barnett, “Quantum formulation of fractional orbital angular momentum,” *Journal of Modern Optics*, vol. 54, no. 12, pp. 1723–1738, 2007.
- [44] H.-C. Huang, “Various angle periods of parabolic coincidence fringes in violation of the bell inequality with high-dimensional two-photon entanglement,” *Phys. Rev. A*, vol. 98, p. 053856, Nov 2018.
- [45] A. C. Dada and E. Andersson, “On bell inequality violations with high-dimensional systems,” *International Journal of Quantum Information*, vol. 9, no. 07n08, pp. 1807–1823, 2011.
- [46] J. Romero, D. Giovannini, D. Tasca, S. Barnett, and M. Padgett, “Tailored two-photon correlation and fair-sampling: a cautionary tale,” *New Journal of Physics*, vol. 15, no. 8, p. 083047, 2013.
- [47] H.-C. Huang, “Quantifiable example of complementarity relation between optical orbital angular momentum and angular position,” *Optics Communications*, 2019.
- [48] S. Oemrawsingh, E. Eliel, J. Woerdman, E. Verstegen, J. Kloosterboer, *et al.*, “Half-integral spiral phase plates for optical wavelengths,” *Journal of Optics A: Pure and Applied Optics*, vol. 6, no. 5, p. S288, 2004.
- [49] J. Leach, E. Yao, and M. J. Padgett, “Observation of the vortex structure of a non-integer vortex beam,” *New Journal of Physics*, vol. 6, no. 1, p. 71, 2004.
- [50] C. Rosales-Guzmán and A. Forbes, *How to shape light with spatial light modulators*. SPIE Press, 2017.

## SUPPLEMENTARY INFORMATION

### A. Schmidt number

There are various ways to quantify the dimensionality of a quantum state including measures such as standard deviations, full width half maximum (FWHM) or more conveniently the Schmidt number or rank ( $K$ ). The Schmidt number quantifies the minimum number of basis states taken from an overcomplete set, required to fully describe a quantum system. For example, in the OAM basis, the product state  $|\ell\rangle|-\ell\rangle$ , for some integer  $\ell$ , can be used to represent a two photon quantum state,

$$|\Psi\rangle = \sum_{\ell=-L}^L \lambda_{\ell} |\ell\rangle |-\ell\rangle, \quad (9)$$

where  $|\lambda_{\ell}|^2$  is the probability of detecting the biphoton state  $|\ell\rangle|-\ell\rangle$ . The Schmidt number of such a state can be obtained from

$$K = \frac{(\sum_{\ell} |\lambda_{\ell}|^2)^2}{\sum_{\ell} |\lambda_{\ell}|^4}. \quad (10)$$

Another convenient measure is the width,  $\Delta\ell$ , of the distribution as two times the square root of its variance

(second central moment), given by

$$\Delta\ell = 2\sqrt{\frac{\sum_{\ell} |\ell|^2 |\lambda_{\ell}|^2}{\sum_{\ell} |\lambda_{\ell}|^2}}. \quad (11)$$

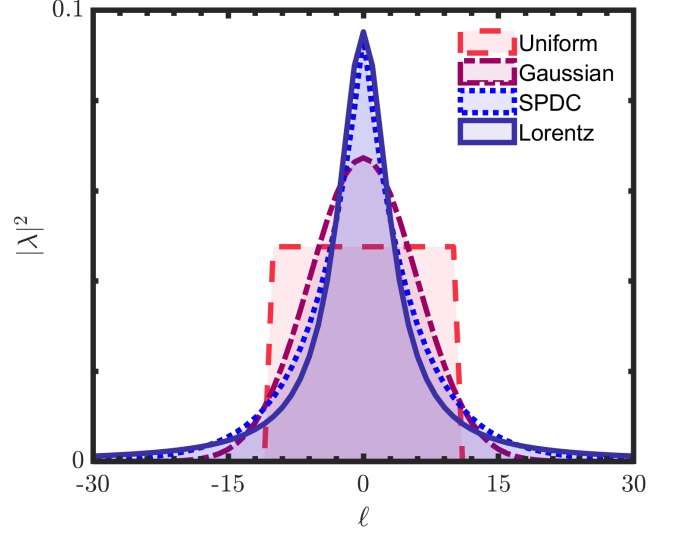


FIG. 5. Examples of various OAM ( $\ell$ ) distributions for a quantum source possessing OAM entanglement.

Both  $K$  and  $\Delta\ell$  and  $\ell$  depend on the shape of the distribution  $|\lambda_{\ell}|^2$ . Examples of various types of distributions for  $|\lambda_{\ell}|^2$  are shown in Fig. 5 for  $K = 21$ . The distributions are: a square distribution, corresponding to a uniform (maximally entangled state) within a given  $\ell$  range, i.e.  $\lambda_{\ell} = 1/\sqrt{2L+1}$ ; a Gaussian (normal) distribution

$$|\lambda_{\ell_g}|^2 \propto \exp\left[-\frac{|\ell|^2}{2\sigma^2}\right], \quad (12)$$

where  $\sigma$  is the standard deviation; a SPDC source [26, 27]

$$|\lambda_{\ell_s}|^2 \propto \left(\frac{2\gamma_S^2}{1+\gamma_S^2}\right)^{|\ell|}, \quad (13)$$

where  $\gamma_S$  is determined by the experimental conditions; and a Lorentz distribution

$$|\lambda_{\ell_L}|^2 \propto \frac{1}{\pi\gamma_L \left(1 + \frac{\ell^2}{\gamma_L^2}\right)}, \quad (14)$$

where  $\gamma_L$  is a scaling parameter.

Note that all distributions in Fig. 5 have the same  $K$  value, but differ in  $\Delta\ell$ , with  $\Delta\ell = 12, 11.8, 14.6$  and  $41.45$  for the square, Gaussian, SPDC and Lorentz distributions, respectively.

### B. Single fractional OAM analyser

A single fractional OAM mode analyser can be represented on the high dimensional Hilbert space using the OAM basis modes  $|\ell\rangle \in \mathcal{H}_\infty$  as

$$|M, \alpha\rangle = \sum_{\ell=-\infty}^{\infty} c_{\ell,M}(\alpha) |\ell\rangle, \quad (15)$$

where the complex coefficients  $c_{\ell,M}(\alpha)$  are computed from the overlap integral  $\int e^{-i\ell\phi} e^{i\Phi_M(\phi;\alpha)} d\phi$ , where  $e^{i\Phi_M(\phi;\alpha)}$  is the azimuthal dependent mode characterizing the analyser orientated at an angle  $\alpha$ . Note that a complete decomposition would require an expansion onto a complete basis that includes the radial component. For brevity, we restrict ourselves to the azimuthal degree of freedom, consistent with [43].

By computing the overlap integral, one arrives at complex amplitudes

$$c_{\ell,M}(\alpha) = -\frac{ie^{-i\ell\alpha} \sin(\mu\pi)}{\pi(M-\ell)}, \quad (16)$$

with  $\mu$  representing the fractional part of the total charge  $M$ . The detection probability for each OAM mode with charge  $\ell$  is therefore

$$P_\ell = |c_{\ell,M}(\alpha)|^2 = \frac{\sin^2(\mu\pi)}{\pi^2(M-\ell)^2}, \quad (17)$$

consistent with probability amplitudes computed in [43] for fractional OAM states.

### C. Superpositions of fractional OAM analyser

We have shown that fractional OAM modes project onto the high dimensional state space of OAM modes with complex amplitudes given by Eq. (16). Next, we tailor new amplitudes and phases by superimposing rotated fractional OAM modes

$$|M, \alpha\rangle_n = \mathcal{N} \sum_{k=0}^{n-1} |M, \beta_k \oplus \alpha\rangle, \quad (18)$$

where  $\mathcal{N}$  is a normalization constant. Each fractional mode in this superposition has the same charge,  $M$ , but is rotated by an angle  $\beta_k \oplus \alpha = \text{mod}\{\beta_k + \alpha, 2\pi\}$  for  $\beta_k = \frac{2\pi}{n}k$ . In the OAM basis, Eq. (18) becomes

$$\begin{aligned} |M, \alpha\rangle_n &= \mathcal{N} \sum_{k=0}^{n-1} \left\{ \sum_{\ell} c_{\ell,M}(\beta_k \oplus \alpha) |\ell\rangle \right\}, \\ &= \mathcal{N} \sum_{\ell} c_{\ell,M}^n(\alpha) |\ell\rangle \end{aligned} \quad (19)$$

where the coefficients  $c_{\ell,M}^n(\alpha)$  are computed from

$$c_{\ell,M}^n(\alpha) = \sum_{k=0}^{n-1} c_{\ell,M}(\beta_k \oplus \alpha). \quad (20)$$

Using Eq. (16) and the condition  $\text{mod}\{\beta_k \oplus \alpha, 2\pi\} = 0$ , we obtain

$$c_{\ell,M}^n(\alpha) = \mathcal{N} c_{\ell,M}(\alpha) \sum_{k=0}^{n-1} e^{i\beta_k \ell}. \quad (21)$$

Since the summation can be evaluated as a geometric series, after some simplification it results in

$$\sum_{k=0}^{n-1} e^{i\beta_k \ell} = e^{-\frac{i\pi\ell(n-1)}{n}} \csc\left(\frac{\pi\ell}{n}\right) \sin(\pi\ell).$$

Therefore the coefficients can be written as

$$c_{\ell,M}^n(\alpha) = \mathcal{N} e^{-\frac{i\pi\ell(n-1)}{n}} A_\ell^n c_{\ell,M}(\alpha). \quad (22)$$

where

$$\begin{aligned} A_\ell^n &= \csc\left(\frac{\pi\ell}{n}\right) \sin(\pi\ell), \\ &= \begin{cases} 0 & \text{mod}\{\frac{1}{2}\ell\beta_{n-1}, 2\pi\} \neq 0 \\ 1 & \text{mod}\{\frac{1}{2}\ell\beta_{n-1}, 2\pi\} = 0 \end{cases}. \end{aligned} \quad (23)$$

Subsequently, the overlap probabilities are  $P_{\ell,n} = |\mathcal{N} A_\ell^n c_{\ell,M}(\alpha)|^2$ . Importantly, the probabilities are independent of  $\alpha$ . Accordingly, the new spectrum has the amplitudes  $|c_{\ell,M}|$ , but following the selection rule  $A_\ell^n$ . Indeed, this new spectrum can be tuned by carefully selecting  $n$ , therefore enabling control of the OAM subspaces.

### D. Spiral imaging of fractional OAM analysers

Our fractional OAM analysers can be decomposed into the OAM basis using entangled photons through digital spiral imaging. In this scheme, one photon from an entangled pair interacts with the analyser while its twin is decomposed in the OAM basis. The entangled photon pair has a biphoton state

$$|\Psi\rangle = \sum_{\ell=-L}^L \lambda_\ell |\ell\rangle |-\ell\rangle, \quad (24)$$

as defined in Eq. (9). The probability amplitude for detecting the  $m$ th OAM mode, given a  $M$  charged fractional mode of  $n$  superpositions, is

$$\begin{aligned} \tilde{c}_m^n(\alpha) &= \mathcal{M} \langle m | \langle M, \alpha |_n | \Psi \rangle, \\ &= \mathcal{M} \sum_{\ell=-L}^L \lambda_\ell \langle m | \ell \rangle \langle M, \alpha |_n | -\ell \rangle. \end{aligned} \quad (25)$$

where  $\mathcal{M}$  is a normalisation constant such that  $\sum_m |\tilde{c}_m^n(\alpha)|^2 = 1$ . Due to the orthonormality of the OAM basis, the overlap  $\langle m | \ell \rangle$  is simply the Kronecker delta function  $\delta_{m,\ell}$ , which evaluates as 0 if  $\ell \neq m$  or 1 if  $\ell = m$ . Since from Eq. (22) we know the expansion



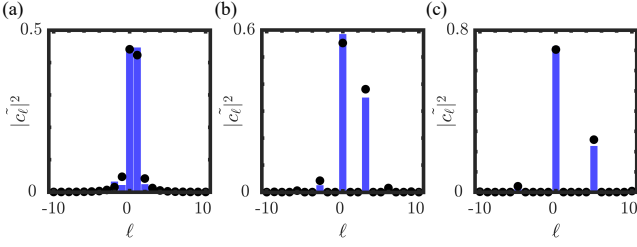


FIG. 6. Measured (bars) and theoretical spectrum (points) for fractional OAM analysers (a)  $|M, \alpha\rangle_n = |0.5, 0\rangle_1$ , (b)  $|M, \alpha\rangle_n = |1.5, 0\rangle_3$ , and (c)  $|M, \alpha\rangle_n = |2.5, 0\rangle_5$  resulting from digital spiral imaging with entangled photons. Here the weightings are modulated by the OAM spectrum of the entanglement source according to Eq. (26).

coefficients for the analyser in terms of the OAM basis,  $\langle M, \alpha | n | \ell \rangle$  evaluates as

$$\begin{aligned} \tilde{c}_m^n(\alpha) &= \mathcal{M} \sum_{\ell=-L}^L \delta_{m,\ell} \lambda_\ell [c_{-\ell}^n(\alpha)]^* \\ &= \mathcal{M} \lambda_m [c_{-m}^n(\alpha)]^* \\ &= \mathcal{M} \lambda_m c_{-m}^n(\alpha). \end{aligned} \quad (26)$$

These new weightings are simply the original coefficients of the analysers modulated by the spectrum of the entangled system. For a maximally entangled state, we obtain the expression  $|\tilde{c}_m^n(\alpha)|^2 = |c_{-m}^n(\alpha)|^2$ , being the original weightings of the analyser, as desired.

In Fig. 6 we show the measured weightings for our SPDC system which has a normally distribution of OAM modes with  $\Delta\ell = 11$  centered at  $\ell = 0$ . We show results for  $|M, \alpha\rangle_n = |0.5, 0\rangle_1, |1.5, 0\rangle_3, |2.5, 0\rangle_5$  for analysers  $n = 1, 3$  and  $5$  in Fig. 6(a),(b) and (c), respectively. It can be seen that the theory and experiment are in good agreement. To obtain these results, two photons where generated from an SPDC source and modulated with SLMs (see experimental setup in Methods section). One SLM was encoded with a fractional OAM mode projecting onto the state,  $|M, 0\rangle_n$ , while the second SLM was encoded with OAM basis modes,  $|\ell\rangle$ .

### E. Detection probability from relative rotations of the analysers

Given a bipartite system of the form of Eq. (24), we want to know what the detection probability is, due to the relative rotations of our fractional OAM analysers acting the entangled photons. Suppose the first analyser projects onto the state  $|M, \theta_1\rangle_n$ , and the second analyser projects on the state  $|M, \theta_2\rangle_n$ . A joint measurement on a two photon system using the two analysers is characterized by the the product state  $|M, \theta_1\rangle_n |M, \theta_2\rangle_n$ . The probability amplitude resulting from such a measurement

is

$$\begin{aligned} C_n(\theta_1, \theta_2) &= \langle \theta_2, M | n \langle \theta_1, M | n | \Psi \rangle \\ &= \sum_{\ell=-\infty}^{\infty} \lambda_\ell \langle M, \theta_1 | n | \ell \rangle \langle M, \theta_2 | n | -\ell \rangle. \end{aligned} \quad (27)$$

Therefore we only need to know how to decompose each of the analysers in the OAM basis to obtain the detection probability for the joint measurements. Using Eq. (22), follows that

$$C_n(\theta_1, \theta_2) \propto \sum_{\ell=-\infty}^{\infty} \underbrace{\lambda_\ell}_{\text{SPDC}} \left[ \underbrace{c_{\ell,M}^n(\theta_1)}_{\text{analyser}} \underbrace{c_{-\ell,-M}^n(\theta_2)}_{\text{analyser}} \right]^*. \quad (28)$$

We use this approach to numerically calculate the detection probabilities  $|C_n(\theta_1, \theta_2)|^2$  by simply calculating the probability amplitudes for each analyser in the OAM basis with a desired rotation  $\theta_{1,2}$  and multiplying them with the coefficients  $\lambda_\ell$  that determine the quantum system being probed.

An alternative approach, can be to compute the overlap integral by considering the modal overlaps in the azimuthal degree of freedom,  $\phi$ , following

$$\langle \theta, M | n | \ell \rangle = \frac{1}{2\pi} \int \exp(-i\Phi_M(\phi; \theta)) \times \exp(i\ell\phi) d\phi$$

, with  $(1/\sqrt{2\pi})\Phi_M(\phi; \theta)$  being the transmission function of the fractional OAM analyser projects onto the state  $|M, \theta\rangle_n$ . We can rewrite probability amplitude  $C_n(\theta_1, \theta_2)$  as an overlap integral given by

$$\begin{aligned} C_n(\theta_1, \theta_2) &= \frac{1}{4\pi} \sum_{\ell=-\infty}^{\infty} \left( \lambda_\ell \iint e^{-i\Phi_M(\phi_1; \theta_1)} e^{i\ell\phi_1} \right. \\ &\quad \times \left. e^{-i\Phi_{-M}(\phi_2; \theta_2)} e^{-i\ell\phi_2} d\phi_1 d\phi_2 \right), \end{aligned} \quad (29)$$

where  $\Phi_{\pm M}(\phi_{1,2}, \theta_{1,2})$  are the phases of the fractional OAM analysers. Since  $e^{-i\Phi_M(\phi_1; \theta_1)}$  has no  $\ell$  dependence, we can introduce the summation into the second integral resulting in

$$\begin{aligned} C_n(\theta_1, \theta_2) &= \frac{1}{2\pi} \int e^{-i\Phi_M(\phi_1; \theta_1)} \left( \int e^{-i\Phi_M(\phi_2; \theta_2)} \right. \\ &\quad \times \left. \frac{1}{2\pi} \sum_{\ell=-\infty}^{\infty} \lambda_\ell e^{i\ell(\phi_1 - \phi_2)} d\phi_2 \right) d\phi_1. \end{aligned} \quad (30)$$

it is convenient to define the periodic function

$$\Lambda(\phi_1 - \phi_2) = \frac{1}{2\pi} \sum_{\ell=-\infty}^{\infty} \lambda_\ell e^{i\ell(\phi_1 - \phi_2)},$$

with angular harmonics  $e^{i\ell(\phi_1 - \phi_2)}$  determined by the co-

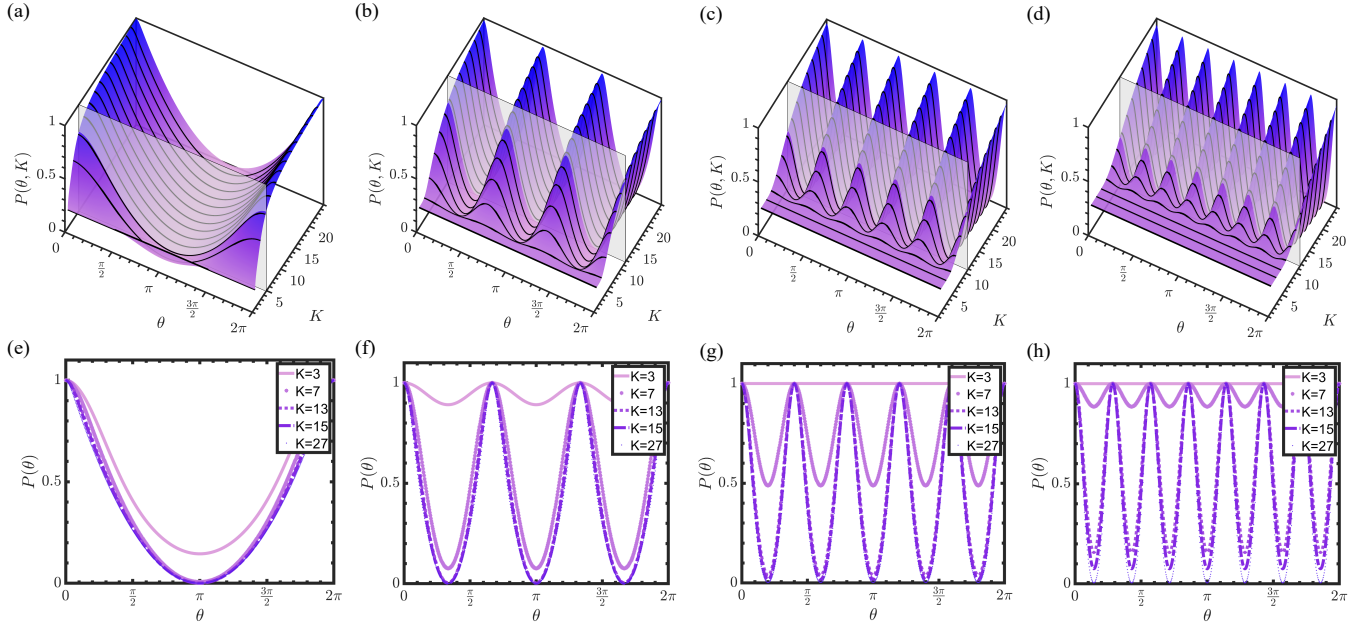


FIG. 7. Simulated normalised probability curves for (a)  $n = 1$ , (b)  $n = 3$ , (c)  $n = 5$  and (d)  $n = 7$ , with fractional OAM  $M = \frac{n}{2}$ , as a function of the relative orientation  $\theta$  between the two analysers and the dimensions,  $K$ , of the entanglement state. The second row of panels (e)-(h) are probability curves for specific  $K$  values for each analyser. The normalisation to unity was performed to illustrate the impact of the dimensions on the visibility. Here, the OAM spectrum shape was assumed to follow a normal (Gaussian) distribution.

efficients  $\lambda_\ell$ , to rewrite  $C_n(\theta_1, \theta_2)$  as

$$C_n(\theta_1, \theta_2) = \frac{1}{2\pi} \int e^{-i\Phi_M(\phi_1; \theta_1)} \left( \int e^{-i\Phi_M(\phi_2; \theta_2)} \Lambda(\phi_1 - \phi_2) d\phi_2 \right) d\phi_1. \quad (31)$$

Notice that the second integral is a convolution between  $\Lambda(\phi_1 - \phi_2)$  and the second analyser. As a example, we consider a maximally entangled state ( $\lambda_\ell := \text{constant}$ ). In this case,  $\Lambda(\phi_1 - \phi_2) = \delta(\phi_1 - \phi_2)$  and therefore

$$C_n(\theta_1, \theta_2) = \frac{1}{2\pi} \int e^{-i\Phi_M(\phi; \theta_1)} e^{-i\Phi_{-M}(\phi; \theta_2)} d\phi.$$

The integral now only depends in the transmission functions of the analysers with an analytical solution found in [44].

We now calculate the probability  $P_n(\theta_1, \theta_2) = |C_n(\theta_1, \theta_2)|^2$  as a function of relative orientation  $\theta = (\theta_1 - \theta_2)$  between the two analysers and the dimensions,  $K$ , of an entangled system with some given OAM spectrum  $|\lambda_\ell|^2$ . The latter is embedded in the function  $\Lambda(\phi_1 - \phi_2)$ . Figures 7(a)-(d) show examples of the probability surfaces assuming a normal (Gaussian) spectrum  $|\lambda_\ell|^2$  for superposition states  $n = 1, 3, 5$  and  $7$ . In the second row of panels, Fig. 7 (e)-(h), examples of the probability curves normalised to unity are shown for several values of dimensionality  $K$ . Here, it can be seen that the frequency of the probabilities as a function of  $\theta$  increases with  $n$ , owing to the  $n$ -fold symmetry in the phase

profiles of the analysers. Crucially, the exact shape and visibility of the curves depends on both the dimensions ( $K$ ) of the state being probed and the number of superpositions ( $n$ ). For all  $n$ s, the visibility for a specific  $K$  shows a decreasing trend as the number of superpositions  $n$  are increased. Therefore the analysers are sensitive to the dimensions of the system.

We also found that the shape of the spectrum affects the measured probabilities, as illustrated in Fig. 8(a)-(d) for square (maximally entangled), normal (Gaussian), SPDC and Lorentz distributions.

Now that we have shown how the detected probabilities depended on the dimensions and superposition states measured, in the following section, we study the relation between the visibility and dimensions quantitatively.

## F. Visibility for different spectra

The visibilities are calculated from detection probabilities resulting from the projections of an entangled state with an initial OAM distribution  $|\lambda_\ell|^2$  onto the states  $|M, 0\rangle_n | -M, \theta\rangle_n$ , where  $\theta \in [0, 2\pi]$  is their relative rotation.

For example, for a square (uniform) distribution and  $n$  superpositions of fractional modes the probability is

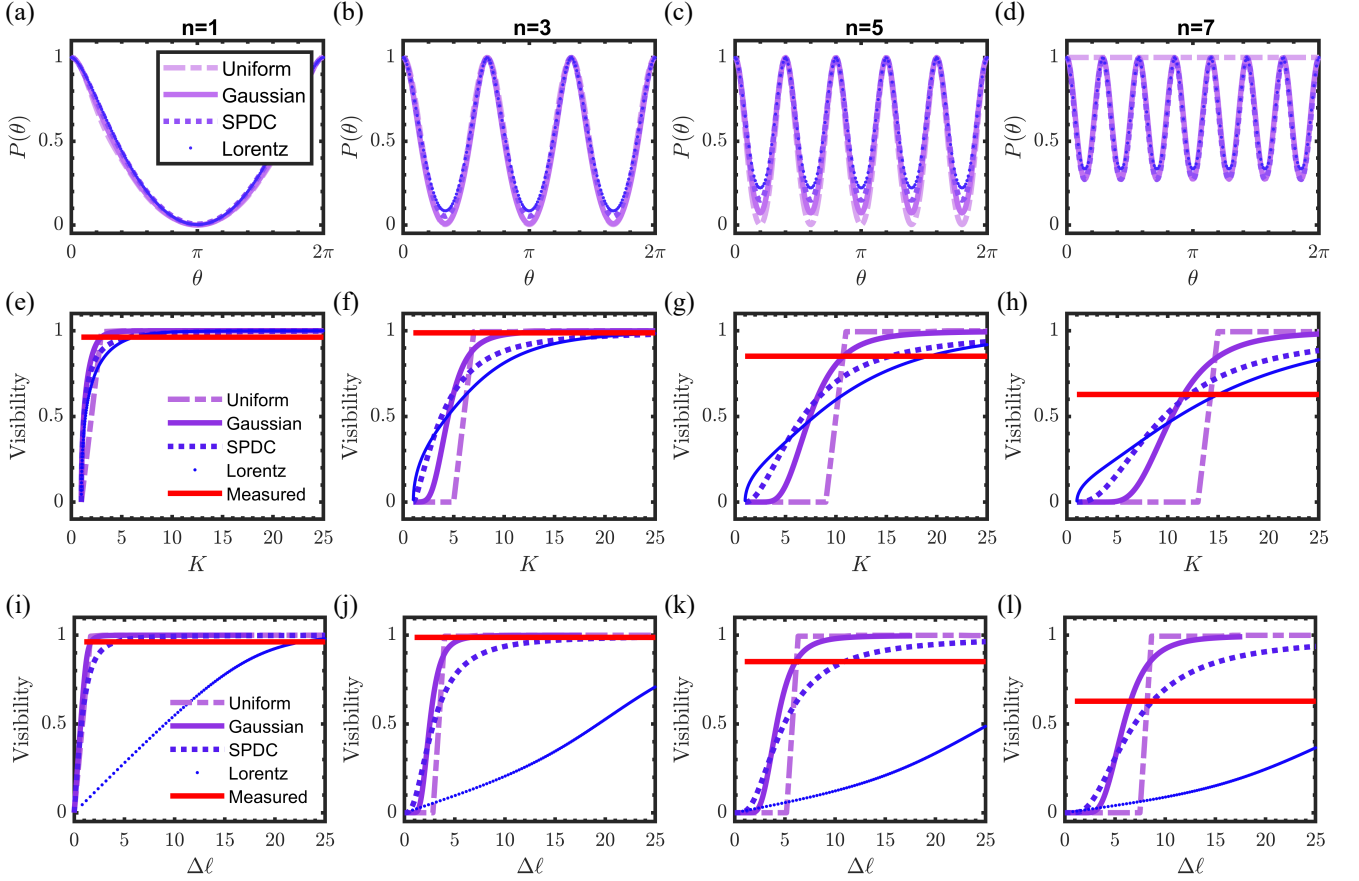


FIG. 8. (a)-(d) Comparison of the probability curves for  $K = 11$  for square (maximally entangled), normal (Gaussian), SPDC and Lorentz spectrum distributions, as a function of the relative orientation  $\theta$  between the two analysers. Each panel corresponds to measurements with fractional OAM superpositions  $n = 1, 3, 5$  and  $7$ , respectively. Corresponding visibilities vs (e)-(h) dimensions,  $K$ , and (i)-(l)  $\Delta\ell$  (two times the standard deviation).

given by[44]

$$P(\theta_1, \theta_2) = |C(\theta_1, \theta_2)|^2 = a \sin^2\left(\frac{M\pi}{n}\right) + \cos^2\left(\frac{M\pi}{n}\right), \quad (32)$$

with  $a = \frac{(\pi(2t-1)-n\theta)^2}{\pi^2}$  for  $\frac{2\pi}{n}(t-1) \leq \theta \leq \frac{2\pi}{n}t$ ,  $t = 1, \dots, n$ , where  $t$  indexes each  $2\pi/n$  period over the range of  $0 \leq \theta < 2\pi$  and  $\theta = \theta_1 - \theta_2$ . This oscillating function results in fringes with a visibility function given by

$$V_n(M) = \frac{1 - \cos^2\left(\frac{M\pi}{n}\right)}{1 + \cos^2\left(\frac{M\pi}{n}\right)}.$$

For  $n = 1$ , parabolic fringes with perfect visibility occur when  $M = \ell + 0.5$  for all OAM integer charges  $\ell$ . In contrast, when  $n > 1$  high visibility fringes occur for only specific choices of  $n$  and  $M$ . That is, parabolic fringes with high visibility ( $V = 1$ ) are expected when  $\text{mod}\left\{M - \frac{n}{2}, n\right\} = 0$ , with the visibility maximised when  $n$  is odd.

Examples of the probabilities for various OAM spectral shapes of a system being probed are shown in Fig.

8 (a)-(d) for a fixed number of dimensions  $K = 11$  for  $n = 1, 3, 5, 7$  with  $M = n/2$ , respectively. As shown, the assumed spectrum can affect the visibility that is measured. Furthermore, the measured visibilities also scale with dimensionality in terms of  $K$  (see Fig. 8 (e)-(h)) and  $\Delta\ell$  (see Fig. 8 (i)-(l)). The visibilities for each analyser and spectrum shape are monotonic with increasing  $K$  ( $\Delta\ell$ ). In particular, for the uniform spectrum (maximal entanglement in  $K$  dimensions) the visibility is 1 above some  $K = d_n$  and zero below this. We further exploit this property to determine the dimensionality of an entanglement system.

### G. Measuring the dimensionality

The main goal of our method is to determine the number of dimensions,  $d$ , that give correlations capable of violating a Bell inequality. In other words, we determine the highest number of Schmidt modes that maximise  $d$ -dimensional entanglement given a system that has access to  $D \geq d$  modes. We achieve this by measuring

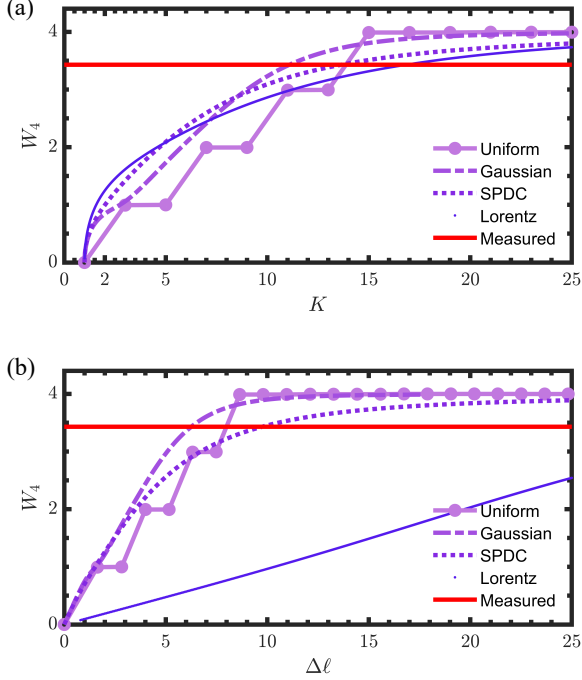


FIG. 9.  $W_4$  parameter for various spectra with respect the Schmidt number  $K$  and the standard deviation  $\Delta\ell$ .

the visibilities resulting from non-local measurements of entangled photons using our tailored analysers. In this section, we discuss 3 different ways in which the visibilities can be used to measure the entanglement dimensions of a quantum system. In the first method, no assumption is made regarding the shape of the spectrum, and yields an estimate for the number of dimensions that approximate  $d$ -dimensional maximal entanglement. In the second and third approaches, the distribution shape is assumed to be known, and provide a better estimate for the dimensionality.

As mentioned in the previous section, for a maximally entangled state (uniform distribution) and analyser  $n$ , there is a number  $d_n$ , so that for  $K > d_n$  the measured visibility will be  $V = 1$ . In particular, for  $n = 1, 3, 5, 7$ , we have  $d_1 = 3$ ,  $d_3 = 7$ ,  $d_5 = 11$  and  $d_7 = 15$ , respectively, and which can be used as an indicator of the number of modes in the investigated system that resemble

a maximally entangled state. Our experimental results are summarised in Table I, where it can be seen we measured visibilities  $V \approx 1$  for analysers  $n = 1, 3$ , meaning that there may be maximal entanglement close to  $d = 5$  dimensions. Importantly, this procedure does not require knowledge about the shape of the OAM distribution.

However, if the OAM spectrum shape is known, the entanglement dimensions can be found by numerically inverting the theoretical visibilities using the results obtained experimentally. That is, given the theoretical visibilities,  $V_n(K)$ , the dimensionality  $K$  can be determined

TABLE I. A summary of the experimental results.

$n$	$d_n$	$V_{\text{measured}}$	$K_{\text{measured}}$	$K_{\text{lower}}$	$K_{\text{upper}}$	$\Delta K$
1	3	$0.96 \pm 0.04$	4.89	4.64	$\infty$	13.28
3	7	$0.99 \pm 0.01$	11.65	8.15	$\infty$	2.42
5	11	$0.85 \pm 0.02$	10.77	11.59	13	0.36
7	15	$0.62 \pm 0.02$	11.59	11.07	11.98	0.22

by minimising  $|V_n^{\text{measured}} - V_n(K)|$ . In our experiment (Table I), we repeated each measurement four times, and calculated the visibility  $V$  and uncertainty  $\Delta V$  as the mean value and standard deviation, respectively. In addition to the uncertainty, we defined  $\Delta V_{\text{bound}}$  as an error tolerance, such that  $|V_n^{\text{measured}} - V_n(K)| \leq \Delta V_{\text{bound}}$ . Using this value, we can compute the upper ( $K_{\text{upper}}$ ) and lower ( $K_{\text{lower}}$ ) bounds for the measured dimensions. We find that as one increases  $n$ , the difference between the upper and lower bounds of the measured dimensions decreases. This occurs when  $|1 - V_n^{\text{measured}}| > \Delta V$ . As a result, the uncertainty  $\Delta K$  is reduced by increasing  $n$ . This works favourably for our scheme, since the visibilities increase monotonically with  $K$ .

In the third method, we first theoretically compute  $W_N(K)$ . Figure 9 shows the calculated  $W_4$  parameter as a function of  $K$  for various spectral shapes. Here, we can see  $W_4$  is a monotonically increasing function for all considered spectra. Second, we determine the dimensionality by numerical inversion of  $W_N(K)$ . Specifically, by minimising  $|W_N(K) - W_N^{\text{measured}}|$ , the dimensions of the system can be inferred. This procedure can be carried out by iterating through the analysers consecutively ( $n = 1, 3, 5, 7, \dots$ ) until the uncertainty in the inferred  $\Delta K$  is less than a previously established value. In this case,  $\Delta K$  is calculated by non-linear error propagation of the measured uncertainty  $\Delta W$ .